

RoofSeg: An edge-aware transformer-based network for end-to-end roof plane segmentation

Siyuan You^a, Guozheng Xu^a, Pengwei Zhou^a, Qiwen Jin^c, Jian Yao^{a,b}, Li Li^{a,b,*}

^a*School of Remote Sensing and Information Engineering, Wuhan University, Wuhan 430079, China*

^b*Wuhan University Shenzhen Research Institute, Shenzhen 518057, China.*

^c*School of Information Engineering, Wuhan University of Technology, Wuhan 430070, China*

Abstract

Roof plane segmentation is one of the key procedures for reconstructing three-dimensional (3D) building models at levels of detail (LoD) 2 and 3 from airborne light detection and ranging (LiDAR) point clouds. The majority of current approaches for roof plane segmentation rely on the manually designed or learned features followed by some specifically designed geometric clustering strategies. Because the learned features are more powerful than the manually designed features, the deep learning-based approaches usually perform better than the traditional approaches. However, the current deep learning-based approaches have three unsolved problems. The first is that most of them are not truly end-to-end, the plane segmentation results may be not optimal. The second is that the point feature discriminability near the edges is relatively low, leading to inaccurate planar edges. The third is that the planar geometric characteristics are not sufficiently considered to constrain the network training. To solve these issues, a novel edge-aware transformer-based network, named RoofSeg, is developed for segmenting roof planes from LiDAR point clouds in a truly end-to-end manner. In the RoofSeg, we leverage a transformer encoder-decoder-based framework to hierarchically predict the plane instance masks with the use of a set of learnable plane queries. To further improve the segmentation accuracy of edge regions, we also design an Edge-Aware Mask Module (EAMM) that sufficiently incorporates planar geometric prior of edges to enhance its discriminability for plane instance mask refinement. In addition, we propose an adaptive weighting strategy in the

*Corresponding author.

Email address: li.li@whu.edu.cn (Li Li)

mask loss to reduce the influence of misclassified points, and also propose a new plane geometric loss to constrain the network training. Extensive experiments demonstrate that the proposed RoofSeg can effectively segment roof planes with accurate edges, minimal misclassified points, and high geometric fidelity, while significantly outperforming the current competitive approaches. We will release the source code of this work at <https://github.com/Li-Li-Whu/RoofSeg>.

Keywords: Roof plane segmentation, 3D building reconstruction, transformer, airborne LiDAR, instance segmentation

1. Introduction

Airborne light detection and ranging (LiDAR) can rapidly acquire large-scale three-dimensional (3D) data with high geometric precision, namely point clouds, which have been commonly employed in 3D building reconstruction (Zhang et al., 2018; Huang et al., 2022; Liu et al., 2024; Sun et al., 2024) at levels of detail (LoD) 2 and 3. Given that the roof structure of a urban building is generally composed of geometrically varied planar patches, roof plane segmentation is a key procedure in 3D building reconstruction. Accurate segmentation of roof planes can significantly improve the final 3D reconstruction quality. However, despite many efforts in roof plane segmentation studies (Khaloo and Lattanzi, 2017; Wang et al., 2019; Liu et al., 2023; Li et al., 2024), extracting accurate roof plane segments from the input point clouds remains challenging for existing 3D reconstruction systems (Yu and Lafarge, 2022).

The existing traditional approaches for roof plane segmentation are predominantly based on point feature grouping mechanism. Guided by some manually designed features (e.g., normal vectors or certain geometric distance), they utilize several grouping techniques, such as region growing (Khaloo and Lattanzi, 2017; Wu et al., 2019), Random SAmple Consensus (RANSAC) (Xu et al., 2015; Canaz Sevgen and Karsli, 2020) or clustering (Miao et al., 2023; Chen et al., 2024), to iteratively group coplanar points with similar features. However, the manually designed features may lack robustness and discriminativity. To solve this problem, some deep learning-based approaches (Zhang and Fan, 2022; Li et al., 2024; Zeng et al., 2025) are proposed to automatically learn more

powerful and representative point features through deep networks. These approaches have demonstrated superior performance compared to traditional approaches. Nevertheless, there are still three unsolved issues in current deep learning-based approaches. The first issue is that most of them can not achieve truly end-to-end roof plane segmentation. They still rely on some geometric voting and clustering techniques (Zhang and Fan, 2022; Li et al., 2024), or other post-processing steps (e.g., edge refinement) (Zeng et al., 2025) to generate the final roof segments. This leads to two main limitations: (1) the inherent difficulty in hyperparameter tuning, and (2) the suboptimal segmentation results caused by error accumulation across multiple intermediate processes. The second issue is that these approaches still struggle to learn instance-discriminative features near the edges, which may lead to inaccurate edge segmentation. The third issue is that they do not fully exploit the geometric characteristics of planes to supervise the network training, which may cause the final plane segments with relatively low geometric fidelity.

To resolve the aforementioned issues, we develop an end-to-end edge-aware transformer-based network, named RoofSeg, for segmenting roof planes from airborne LiDAR point clouds. Inspired by transformers (Cheng et al., 2021; Schult et al., 2023; Lai et al., 2023; Roh et al., 2024) for instance segmentation, we utilize a set of plane queries, learned from transformer-based encoder-decoder architecture, to directly detect the potential planes and predict their instance masks from the point clouds. Thus, we can avoid parameter-sensitive intermediate processing and enable end-to-end roof plane segmentation. To achieve accurate segmentation near the edge regions, we design an Edge-Aware Mask Module (EAMM) for further plane mask refinement. Specifically, we utilize the tangent distances from edge points to the predicted initial plane as the key geometric cues to enhance the learning of edge features, thereby improving the instance discriminability of points near the edges. Subsequently, based on the learned edge-aware point features, the EAMM can predict refined plane masks with accurate edges. Moreover, we propose a novel loss function for supervising the plane mask predictions. Based on the conventional mask loss formulation, we introduce an adaptive weighting strategy to eliminate the influence of misclassified points. To ensure the geometric fidelity of the predicted

plane segments, we design a plane geometric loss to constrain the network training. The extensive experimental results on three benchmarks proves that the proposed RoofSeg generates the roof plane segmentation results with accurate edges, minimal misclassified points and high geometric fidelity, while surpassing the existing competitive approaches. The main contributions of this work are concluded as bellow:

- An end-to-end edge-aware transformer-based network, named RoofSeg, is developed for segmenting roof planes from airborne LiDAR point clouds in this work. Without any carefully designed clustering or post-processing method, RoofSeg can detect all the potential planes and predict their instance masks from 3D point clouds.
- To address the challenge of accurate edge segmentation, we design an Edge-Aware Mask Module (EAMM) that integrates the critical geometric priors to enhance the discriminative edge features learning, which facilitates the further plane mask refinement.
- Based on the existing instance mask loss formulation, we propose a novel loss function that incorporates the adaptive weighting strategy and plane geometric constraint, to ensure the plane mask predictions with minimal misclassified points and high geometric fidelity.
- The extensive experiments conducted on three benchmarks demonstrate that our network achieves the new state-of-the-art performance compared to the current leading approaches.

2. Related work

In general, the existing approaches developed for segmenting roof planes can be classified as two categories, namely handcrafted features-based and deep-learning-based approaches. Moreover, we discuss some end-to-end transformers for instance segmentation, which has significantly inspired our work.

2.1. Handcrafted feature-based approaches

We classify the current handcrafted features-based approaches as four categories: region growing-based, model-fitting-based, clustering-based and optimization-based approaches.

Region growing-based approaches (Vo et al., 2015; Khaloo and Lattanzi, 2017; Wu et al., 2019; Poux et al., 2022; Wang et al., 2023c; Chen et al., 2025) gradually grow the planar patches based on some initial seeds, according to certain geometric growing criteria. Vo et al. (2015) proposed to split initial points into octree-based voxels and extract features of each voxel based on point normal analysis, then they performed voxel-based growing to generate the plane segments. To achieve robust normal estimation, Khaloo and Lattanzi (2017) applied statistical outlier analysis to detect and remove outliers from the neighborhood of each point. Furthermore, Wang et al. (2023c) proposed a robust estimator-based Principal Component Analysis (PCA) for normal estimation to improve efficiency while ensuring accuracy. Chen et al. (2025) first segmented points into hypervoxel with varied scales, and then performed average distance analysis to split the non-planar voxels. After that, they applied an improved region growing algorithm to generate the fine plane segments. Nevertheless, these approaches tend to fail in the edge regions, because of their sensitivity to the parameter setting in the growing criteria.

Model-fitting-based approaches can be classified into two categories: Hough Transform (HT)-based (Overby et al., 2004; Liu et al., 2005; Tarsha-Kurdi et al., 2007) and RANSAC-based approaches (Schnabel et al., 2007; Xu et al., 2015; Li et al., 2017; Canaz Sevgen and Karsli, 2020; Xu and Li, 2023; Cao et al., 2025). HT-based approaches attempt to estimate the best plane models that maximally matches input points in the parameter space, then they allocate points to their nearest plane for generating plane segments. However, according to Tarsha-Kurdi et al. (2007), these approaches are less efficient than RANSAC-based approaches and also yield inferior segmentation accuracy. RANSAC-based approaches randomly sample points for plane fitting, and then determine the best fitted plane with the most inliers. Xu et al. (2015) added a weighted loss function, based on two geometric constraints, into RANSAC for higher-quality plane fit-

ting. [Canaz Sevgen and Karsli \(2020\)](#) improved RANSAC by using an outlier-detecting algorithm to remove unreliable sampling points. [Cao et al. \(2025\)](#) introduced a point filtering method into the RANSAC for eliminating the noises, and then applied Kd-Tree algorithm to remove the non-planar points for segmentation refinement. Nevertheless, these approaches are prone to generate spurious planar patches when handling roofs with complex structures, as the algorithms are prone to converge to the local optima.

Clustering-based approaches ([He et al., 2013](#); [Czerniawski et al., 2018](#); [Wang et al., 2019](#); [Cao et al., 2022](#); [Miao et al., 2023](#); [Chen et al., 2024](#)) segment roof planes by using some clustering techniques. For example, [He et al. \(2013\)](#) first extracted line segments from LiDAR point clouds, and then performed line-based clustering in the spectral space to produce the optimal fitted plane segments. [Czerniawski et al. \(2018\)](#) applied 6D Density Based Spatial Clustering of Applications with Noise (DBSCAN) to group points in both coordinate and normal vector spaces. Besides, [Cao et al. \(2022\)](#) proposed a Fast Euclidean Clustering (FEC) method to reduce the computational complexity of conventional Euclidean Clustering (EC). [Chen et al. \(2024\)](#) first extracted collision points in boundaries. Then, they used adaptive EC method to generate initial clusters and reinserted the collision points to derive complete plane segments. However, these approaches heavily rely on the fine-tuned parameters, such as clustering radius, and are limited by the low quality of handcrafted features.

Optimization-based approaches ([Yan et al., 2014](#); [Gu et al., 2017](#); [Li et al., 2020](#); [Wang and Ji, 2021](#); [Yu and Lafarge, 2022](#); [Liu et al., 2023](#); [Xu et al., 2025](#)) attempt to minimize certain carefully designed energy function for refining segmentation results produced by the above mentioned approaches. [Yan et al. \(2014\)](#) constructed a global multi-label energy function to measure the quality of plane segments, and optimized the energy function with graph cuts technique ([Boykov and Veksler, 2006](#)). In addition, [Yu and Lafarge \(2022\)](#) proposed to optimize a multi-objective energy function in an efficient mechanism with five geometric operators. However, the optimization processes of these approaches are highly time-consuming and resource-intensive. To alleviate that, [Li et al. \(2020\)](#), [Liu et al. \(2023\)](#) and [Xu et al. \(2025\)](#) shifted focus from global to local domains,

specifically targeting at edge regions. They gradually refined edges until obtaining the optimal edge point assignment with minimal energy cost. Yet, they still require setting complex convergence criteria to terminate the optimization of energy functions.

2.2. Deep learning-based approaches

With the rapid advancement of deep learning in recent years, several deep learning-based approaches have been developed for segmenting primitive instances (Jiang et al., 2020; Huang et al., 2021; Yan et al., 2021; Li et al., 2023; Wang et al., 2023b; Fang et al., 2025) or roof planar patches (Zhao et al., 2022; Zhang and Fan, 2022; Li et al., 2024; Zeng et al., 2025) from 3D point clouds. Generally, they first utilized deep networks for learning more robust feature representations from point clouds. After that, they applied certain feature grouping technique to generate the final segments. PrimitiveNet (Huang et al., 2021) combined a high-resolution embedding network with a discriminator module to jointly learn explicit and implicit point-wise features, which are robust in distinguishing between different primitives. HPNet (Yan et al., 2021) designed a multi-branch descriptor module to extract hybrid feature representations integrating semantic information, geometric consistency and local smoothness. Then, a mean-shift clustering module is applied to produce the segmentation results. However, these approaches specifically focus on segmenting primitive instances rather than roof planes. To fill this gap, Zhang and Fan (2022) proposed a joint-learning network for segmenting roof planes from point clouds. They first captured semantic and instance features for each point, and then fused them to obtain high-dimensional embedding features. In training phase, they ensured that the learned features of coplanar points are similar in embedding space, thus facilitating the next clustering process. Based on that, Li et al. (2024) designed a three-branch network to achieve further improvement. In the first branch, they identified and extracted edge points from point clouds. In the latter two branches, they grouped non-edge points in both Euclidean and Embedding spaces to produce coarse plane segments. At last, they allocated edge points to the nearest planes to generate complete segments. Zeng et al. (2025) proposed an improved superpoint-based transformer for extracting roof plane segments. They designed a novel strategy for generating superpoints with high quality, and

input them with multiple manually designed features into the network for generating initial plane segments. Then, they applied traditional post-processing techniques, namely plane completion and edge refinement, to optimize the segmentation results. Nevertheless, these deep learning-based approaches still can not perform truly end-to-end segmentation, resulting in inevitable accumulation of errors throughout intermediate processes. In addition, they still can not learn instance-discriminative features for edge points.

2.3. End-to-end transformers

Transformer, firstly proposed by [Vaswani et al. \(2017\)](#) for Natural Language Processing (NLP), has also achieved remarkable success in vision fields, due to its powerful attention mechanism. Recently, some end-to-end transformers ([Cheng et al., 2021, 2022](#); [Schult et al., 2023](#); [Sun et al., 2023](#); [Lai et al., 2023](#); [Roh et al., 2024](#)) have been proposed for segmentation in 2D or 3D domain, and have achieved outstanding performance. Mask2Former ([Cheng et al., 2022](#)) is the first end-to-end universal architectures developed for 2D image segmentation. Through cross-attention between query features decoded by transformer and pixel-wise features extracted by backbone, it can simultaneously produce instance, semantic, and panoptic masks to support multiple tasks. Building upon this foundation, several effective frameworks ([Schult et al., 2023](#); [Sun et al., 2023](#); [Roh et al., 2024](#)) were subsequently designed for 3D instance segmentation. Mask3D ([Schult et al., 2023](#)) applies 3D U-net backbone for point feature extraction in multi-level resolutions, and gradually uses them to interact with the queries in transformer decoder for instance mask prediction. SPFormer ([Sun et al., 2023](#)) first aggregates point features to generate a set of superpoints. Then, it captures instance information for each query with superpoints cross-attention. However, these works still lack accuracy and robustness in edge segmentation. To fill this gap, [Roh et al. \(2024\)](#) proposed an edge-aware transformer. It applies an edge prediction module to identify the edge points in point clouds, thus enhancing the recognition of edge information in mask prediction. Nevertheless, this edge-aware mechanism is relatively implicit and merely provides limited improvements. Inspired by the aforementioned works, we decide to develop an end-to-end edge-aware transformer-based network for roof plane segmentation in this paper.

3. Our approach

The architecture of our network (RoofSeg) is illustrated in Fig. 1. Taking the original point clouds as inputs, RoofSeg can directly predict the roof segments with the accurate plane label for each point. Firstly, multi-scale point features are captured by a feature extraction backbone based on PointNet++ (Qi et al., 2017), while the plane query embeddings \mathbf{Q}_{emb} are simultaneously generated with K query points downsampled from point clouds. Then, the Query Refinement Decoders (QRD) are applied for hierarchically integrating multi-scale contextual information into the \mathbf{Q}_{emb} , and thus deriving refined query features \mathbf{Q}_{ref} . After that, the initial plane masks are produced by interacting the \mathbf{Q}_{ref} with full resolution point features, namely \mathbf{F}_1 , which are also used to predict edge mask in the edge prediction branch. Subsequently, we design an Edge-Aware Mask Module (EAMM) to further refine plane masks by incorporating the geometric priors into the edge features. In training phase, each refined mask with its binary class (positive or negative), predicted by the query semantic branch based on \mathbf{Q}_{ref} , is applied for bipartite matching with the ground truth to suppress duplicate predictions. During inference, all positive refined masks are merged to generate the final segmentation results.

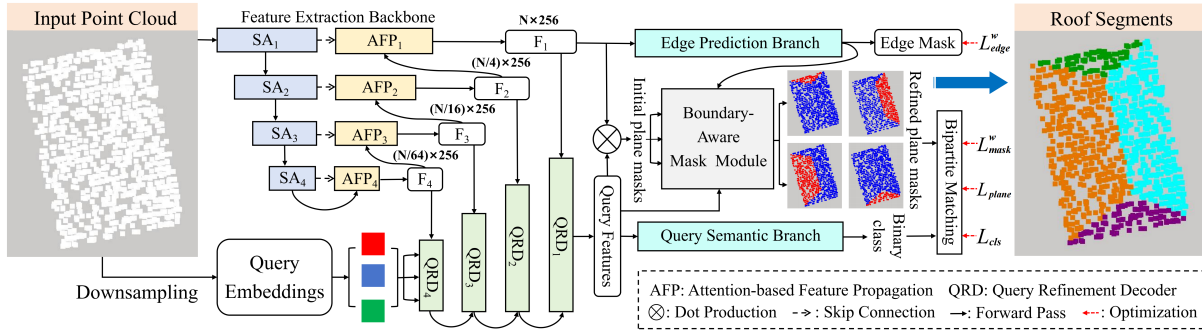


Figure 1: The overview of the end-to-end edge-aware transformer-based network (RoofSeg). Notably, the outputs of each QRD are used for plane mask prediction. For readability, these processes are omitted in this figure.

3.1. Point feature extraction

PointNet++ (Qi et al., 2017) is a prevalent feature extraction backbone for processing 3D point clouds. Its hierarchical architecture, composed of Set Abstraction (SA) and Feature Propagation (FP) modules, can effectively extract point features that integrate both

local and global information. Based on that, we introduce attention mechanism into the FP modules to learn more robust features through point-wise self-attention operations.

Point set abstraction. The input point clouds can be donated as $\mathbf{P} = \{\mathbf{p}_i\}_{i=1}^N$, where N denotes the count of input points. We take the spatial coordinates of \mathbf{P} as its initial features $\mathbf{F}_{init} \in \mathbf{R}^{N \times 3}$. Then, four standard SA modules are employed to progressively perform point downsampling and feature aggregation, with a consistent sampling scale of 1/4 at each level. In this way, the global information are gradually encoded into the features of downsampled points.

Attention-based feature propagation. To recover the point features across different scales, we employ four Attention-based Feature Propagation (AFP) layers for feature decoding. In each layer, as shown in Fig. 2 (left), the low resolution features and the skip connection features (from the associated SA layer) are fed into the standard FP layer for generating upsampled features. Then, an attention-based module is applied to learn point-wise correlations, thus facilitating more robust feature propagation. Through four AFP layers, we derive multi-scale point features with 256 dimensions, denoted as $\mathbf{F}_{multi} = \{\mathbf{F}_l \in \mathbf{R}^{(N/4^{l-1}) \times 256}\}_{l=1}^L$, where $L = 4$ refers to the layer numbers.

3.2. Plane query generation and refinement

Inspired by query-based transformers for instance segmentation, we attempt to utilize a fixed number of queries to gain the information of potential planes included in the roof point clouds.

Query embedding generation. Through Farthest Point Sampling (FPS) method, we primarily sampled K query points from the initial point clouds. This sampling method guarantees globally maximized sampling coverage. After that, we encode the spatial coordinates of query points with the Fourier encoding (Misra et al., 2021) to generate initial query embeddings $\mathbf{Q}_{emb} \in \mathbf{R}^{K \times 256}$. Notably, compared to traditional positional encoding designed for ordered data (e.g., images or text), Fourier encoding demonstrates superior performance in processing unordered and unstructured point clouds (Schult et al., 2023).

Hierarchical query refinement. To encourage the plane information to be accu-

rately learned, we apply four query refinement decoders to gradually integrate the multi-scale information from \mathbf{F}_{multi} into the query embeddings \mathbf{Q}_{emb} . Each decoder, as shown in Fig. 2 (right), is built on the classic transformer block, including two attention layers (each followed by a norm layer) and a feed forward network. The first attention layer of the l -th decoder is applied for facilitating information interaction between plane queries $\mathbf{Q}_l \in \mathbf{R}^{K \times 256}$ and point features $\mathbf{F}_l \in \mathbf{R}^{(N/4^{l-1}) \times 256}$ based on the standard cross-attention operation. This process can be described as:

$$\mathbf{Q}_{att} = softmax(\frac{QK^T}{\sqrt{D}})V, \quad (1)$$

where Q refers to the query vectors linearly projected by \mathbf{Q}_l . K and V refer to the key and value vectors linearly projected by \mathbf{F}_l . D refers to the fixed feature dimension, which is 256 for all vectors. \mathbf{Q}_{att} represents the cross-attention-based query features. After that, \mathbf{Q}_{att} is concatenated with \mathbf{Q}_l , and fed into the self-attention layer, where inter-query communications are further enhanced, thereby inherently suppressing redundant predictions of the same plane instance. Finally, through residual connection with layer normalization, followed by a feed forward network, the decoder can output the ultimate refined query features $\mathbf{Q}_{ref}^l \in \mathbf{R}^{K \times 256}$, which are used for predicting plane masks in the subsequent step.

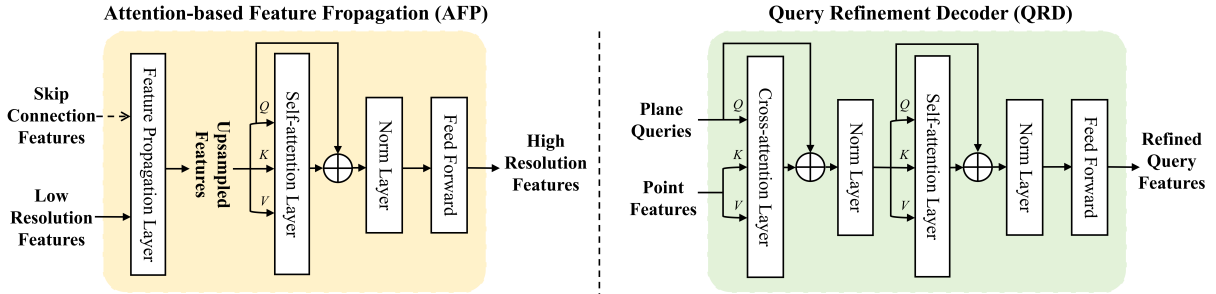


Figure 2: The illustration of the Attention-based Feature Propagation (AFP) and Query Refinement Decoder (QRD). Q , K and V denotes the standard query, key and value embeddings produced for the subsequent attention operation.

3.3. Edge-aware mask generation

Based on the refined query features \mathbf{Q}_{ref} and full resolution point features \mathbf{F}_1 , we generate the initial plane mask for each plane query, and predict the edge mask simultaneously. Then, through an edge-aware mask module, we achieve further plane mask refinement with critical edge geometric cues.

Initial plane masks. We compute the dot products between $\mathbf{Q}_{ref} \in \mathbf{R}^{K \times 256}$ and $\mathbf{F}_1 \in \mathbf{R}^{N \times 256}$ to generate an affinity matrix $\mathbf{A} \in \mathbf{R}^{K \times N}$, where each element a_{ij} represents the affinity between the i -th plane query and j -th point. This process can be formulated as below:

$$\mathbf{A} = \{a_{ij} = (\mathbf{Q}_{ref} \otimes \mathbf{F}_1^T)_{ij}\}. \quad (2)$$

Through a sigmoid activation function, \mathbf{A} is then mapped to a normalized value space, where $a_{ij} \in [0, 1]$. After that, we binarize the matrix using a threshold of 0.5, thereby deriving binary plane masks \mathbf{M}_{plane} , where a value of 1 indicates points inside the plane, and 0 denotes those outside. This procedure can be expressed as:

$$\mathbf{M}_{plane} = \{m_{ij} = [\text{sigmoid}(\mathbf{A}) \geq 0.5]_{ij}\}, \quad (3)$$

where $[\cdot]$ refers to an indicator for returning 1 or 0, according to whether the condition is satisfied or not.

Edge masks. To detect the edge points included in point clouds, we input \mathbf{F}_1 into the edge prediction branch, which is essentially a Multi-Layer Perceptron (MLP) with output dimension $D_{out} = 1$, for predicting the edge probability heatmap $\mathbf{H}_{edge} \in \mathbf{R}^{N \times 1}$. Then, similar to the plane mask generation, we apply normalization and binarization to \mathbf{H}_{edge} for producing the binary edge mask \mathbf{M}_{edge} .

Edge-aware plane masks. As shown in Fig. 3, the initial plane mask appears inaccurate segmentation in edge regions. This is because the edge features learned by the network still lack sufficient discriminability and robustness. To address this limitation, we consider to enhance edge features by introducing the point-to-plane distance, which serves as a discriminative geometric cue for identifying point-plane associations. Built upon this

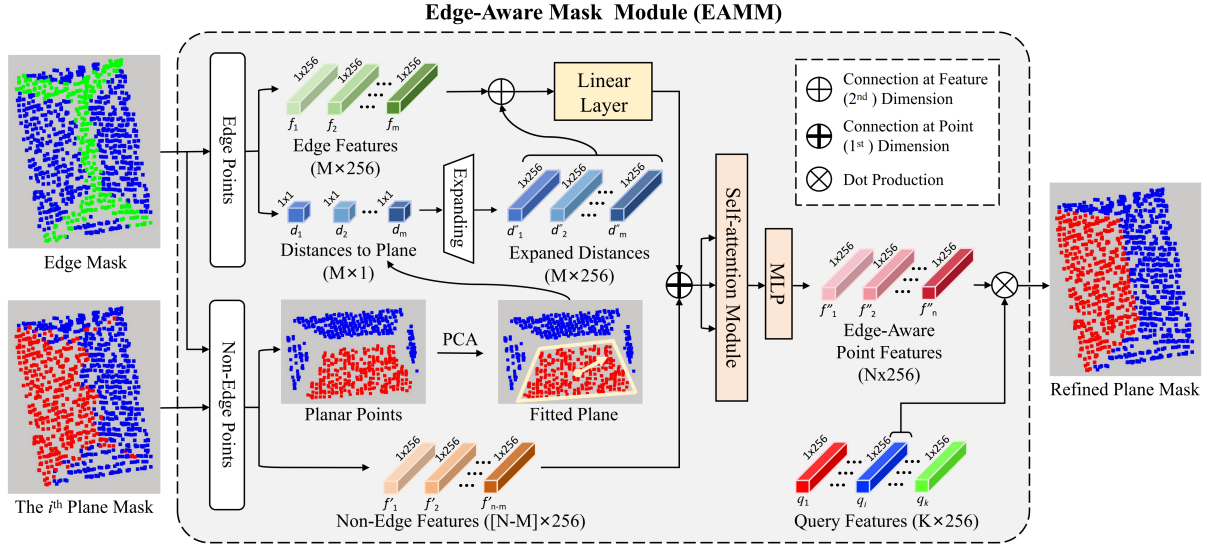


Figure 3: The illustration of the Edge-Aware Mask Module (EAMM). The green dots in the edge mask represent the predicted edge points in point clouds. The red and blue dots denote the points inside and outside the predicted plane. For simplicity, this figure only illustrates the refinement of one plane mask as an example.

insight, an Edge-Aware Mask Module (EAMM) is designed for plane mask refinement. Specifically, we first extract M edge points, denoted as $\mathbf{E} = \{e_i\}_{i=1}^M$, with their initial features $\mathbf{E}_{init} \in \mathbf{R}^{M \times 256}$ from the edge mask \mathbf{M}_{edge} and point-wise features \mathbf{F}_1 . Then, we extract the planar interior points (without edge points), which are used for robust plane estimation through Principal Component Analysis (PCA). Based on that, the tangent distance d_i from each edge point e_i to the fitted plane is computed and expanded to the distance vector with 256 dimensions. In this way, we can acquire distance features $\mathbf{D}_{edge} \in \mathbf{R}^{M \times 256}$ of all edge points. After that, \mathbf{E}_{init} and \mathbf{D}_{edge} are connected and input into a full connection linear layer to generate the fused edge features $\mathbf{E}_{fuse} \in \mathbf{R}^{M \times 256}$. We then merge \mathbf{E}_{fuse} with the non-edge features $\mathbf{F}_{non_edge} \in \mathbf{R}^{(N-M) \times 256}$ and input them into a self-attention module for inter-point interaction, thus producing the edge-aware point features $\mathbf{F}_1^{ea} \in \mathbf{R}^{N \times 256}$. Finally, the refined plane mask is generated based on \mathbf{F}_1^{ea} and the query feature q_i associated to the initial plane mask.

Plane mask merging. Given that the number of predicted plane masks may exceed the ground truth, we categorize the plane masks into two classes (positive or negative), according to their semantic scores, denoted as $\mathbf{S}_{cls} = \{s_i \in [0, 1]\}_{i=1}^K$, predicted by the

query semantic branch. After that, we select positive masks ($s_i \geq 0.5$), and merge them together to generate the final plane mask \mathbf{M}_{final} . To achieve that, we allocate the most suitable plane label l_{p_j} for point $p_j \in \mathbf{P}$, by finding the maximum confidence score it has across all positive masks. The confidence score of p_j in each mask is measured by both the semantic score of mask and point-to-plane affinity. This process can be expressed as:

$$\mathbf{M}_{final} = \{l_{p_j} = \arg \max_{1 \leq i \leq N_{pos}} (s_i \cdot a_{ij})\}_{j=1}^N, \quad (4)$$

where N_{pos} denotes the number of positive plane masks. s_i refers to the semantic score of the i -th positive mask, while $a_{ij} \in \mathbf{A}$ refers to the affinity between p_j and the i -th predicted positive plane.

3.4. Loss functions

RoofSeg is trained with a unified loss function \mathcal{L} , which is a combination of four parts: adaptive weighting plane mask loss \mathcal{L}_{mask}^w , plane geometric loss \mathcal{L}_{plane} , semantic class loss \mathcal{L}_{cls} and edge mask loss \mathcal{L}_{edge}^w . We formulate it as follows:

$$\mathcal{L} = \mathcal{L}_{mask}^w + \mathcal{L}_{plane} + \mathcal{L}_{cls} + \mathcal{L}_{edge}^w. \quad (5)$$

Plane mask loss. Classic instance mask loss \mathcal{L}_{mask} , proposed by (Schult et al., 2023), consists of the binary cross-entropy loss \mathcal{L}_{BCE} and the Dice loss \mathcal{L}_{Dice} . It can be formulated as:

$$\mathcal{L}_{mask} = \mathcal{L}_{BCE} + \mathcal{L}_{Dice}. \quad (6)$$

However, this loss formulation demonstrates limited effectiveness in suppressing outliers within predicted masks, as shown in Fig. 4, since all points contribute equally to the loss computation. To overcome this limitation, our objective is to modify \mathcal{L}_{mask} by incorporating an adaptive weighting mechanism that imposes stronger constraints on outliers. In this way, the network is encouraged to predict plane segments with minimal misclassified points (outliers). Specifically, we first perform neighborhood analysis based on the predicted plane mask. For each point $p_j \in \mathbf{P}$, we calculate N_{dif}^j , which refers to

the number of neighbors with labels different from p_j . When N_{dif}^j exceeds half of the total N_{nbr} neighbors, we identify p_j as a potential outlier. Through this process, we can obtain N_{out} detected outliers, denoted as $\mathbf{O} = \{o_i\}_{i=1}^{N_{out}}$, before loss computation. Then, the weight of each o_i is calculated through the multiplication of a global factor (i.e., the ratio of inlier count $N - N_{out}$ to outlier count N_{out}) and a local factor (i.e., the ratio of N_{dif}^j to N_{nbr}), while the weights of other points are set to all ones. This outlier detection and adaptive weighting method is specified in Algorithm 1, where $\text{KNN}(\cdot)$ refers to the K Nearest Neighbors searching algorithm, and Ind refers to the neighbor indices of the point p_j . The adaptive weighting plane mask loss \mathcal{L}_{mask}^w can be formulated as follows:

$$\mathcal{L}_{mask}^w = \mathcal{L}_{BCE}^w + \mathcal{L}_{Dice}^w, \quad (7)$$

$$\mathcal{L}_{BCE}^w = -\frac{1}{N} \sum_{j=1}^N w_j [l_{gt_j} \cdot \log(a_j) + (1 - l_{gt_j}) \cdot \log(1 - a_j)], \quad (8)$$

$$\mathcal{L}_{Dice}^w = 1 - \frac{2 \sum_{j=1}^N w_j (a_j \cdot l_{gt_j}) + \epsilon}{w_j (\sum_{j=1}^N a_j + \sum_{j=1}^N l_{gt_j}) + \epsilon}, \quad (9)$$

$$w_j = \begin{cases} \frac{N - N_{out}}{N_{out}} \cdot \frac{N_{dif}^j}{N_{nbr}}, & \text{if } p_j \in \mathbf{O}, \\ 1, & \text{otherwise,} \end{cases} \quad (10)$$

where w_j refers to the weight of the j -th point. a_j represents the affinity of the j -th point in the predicted plane mask. l_{gt_j} refers to the label of the j -th point in the ground truth mask. $\epsilon = 1$ acts as a smoothing term to prevent division by zero.

Plane geometric loss. In the current studies for instance segmentation, the geometric characteristics of instance are not sufficiently considered to constrain the network training, which may lead to the predicted instance segments with low geometric fidelity. To overcome this disadvantage, we naturally consider to add the plane geometric constraints, namely point-to-plane distance, into the network training to ensure the high geometric fidelity of the plane predictions. For each predicted mask $\mathbf{M} = \{m_j\}_{j=1}^N$, we extract in-plane points, denoted as $\mathcal{P} = \{p_j \in \mathbf{P} \mid m_j = 1\}$, and apply PCA to fit the planar parametric equation based on in-plane points excluding outliers. Then, we compute

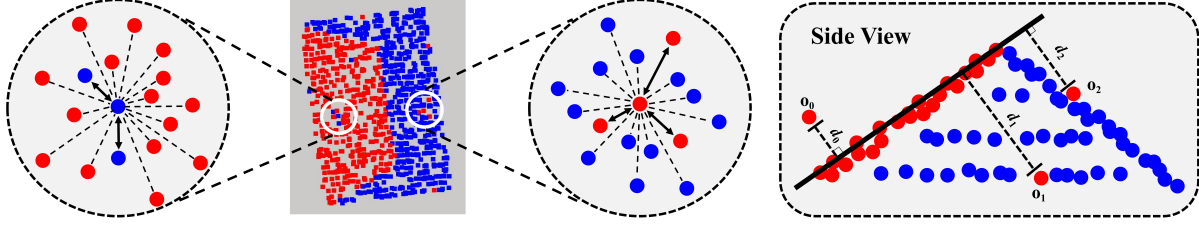


Figure 4: The illustration of outliers. The red and blue dots represent the predicted in-plane points (with label 1) and out-of-plane points (with label 0). In highlighted circles, the dashed lines refer to the mismatching with inconsistent labels, while the double-headed solid lines refer to the correct matching with consistent labels. The dots located at circle centers represent the detected outliers. In side view, the long solid line denotes the fitted plane. The o_0 , o_1 and o_2 represent three outliers existed in the predicted in-plane points.

Algorithm 1 Outlier detection & adaptive weighting method.

Inputs: Point clouds \mathbf{P} ; Plane mask $\mathbf{M} = \{m_j\}_{j=1}^N$; Number of neighbors N_{nbr} .

Outputs: Detected outliers \mathbf{O} ; Weights of all points $\mathbf{W} = \{w_1, \dots, w_N\}$.

```

1: Initialization: An empty set  $\mathbf{O}$ ; A weight array  $\mathbf{W} = \{w_1, \dots, w_N\}$  with all zeros.
2: for  $j = 0$  to  $N$  do
3:   set  $l_j = m_j$ ; calculate  $Ind = \text{KNN}(p_j, \mathbf{P}, N_{nbr})$ ; set  $N_{dif}^j = 0$ 
4:   for  $i$  in  $Ind$  do
5:     set  $l_i = m_i$ 
6:     if  $l_i == l_j$  then continue
7:     else set  $N_{dif}^j = N_{dif}^j + 1$ 
8:     end if
9:   end for
10:  if  $N_{mis} > N_{nbr}/2$  then
11:    insert  $p_j$  to  $\mathbf{O}$ ; set  $w_j = N_{dif}^j / N_{nbr}$ 
12:  end if
13: end for
14: calculate  $N_{out} = |\mathbf{O}|$ 
15: for  $j = 1$  to  $N$  do
16:   if  $w_j == 0$  then set  $w_j = 1$ 
17:   else set  $w_j = (N/N_{out} - 1) \cdot w_j$ 
18:   end if
19: end for
20: return  $\mathbf{O}$ ,  $\mathbf{W}$ .

```

the plane geometric loss, which can be formulated as:

$$\mathcal{L}_{plane} = \frac{1}{|\mathcal{P}|} \sum_{p_j \in \mathcal{P}} \text{Dist}(p_j, \Pi), \quad (11)$$

where $Dist(\cdot)$ refers to point-to-plane distance, Π denotes the fitted plane. It should be noted that this loss formulation can also enhance the suppression of outliers. This is because, compared to in-plane points, the outliers generally exhibit larger distances to the fitted plane, as illustrated in Fig. 4 (right).

Bipartite matching. To eliminate the duplicated predictions, before loss calculation, we allocate the most suitable plane mask prediction to each ground truth mask through bipartite matching (Schult et al., 2023). Firstly, we match K predicted plane masks with N_{gt} ground truth masks, thus deriving $K \times N_{gt}$ matched mask pairs. Then, for each mask pair, we compute its matching cost \mathcal{C}_{match} as:

$$\mathcal{C}_{match} = \mathcal{L}_{mask}^w(\mathbf{M}, \hat{\mathbf{M}}) + \mathcal{L}_{plane}(\mathbf{M}) - \mathbf{S}_{cls}^{\mathbf{M}}, \quad (12)$$

where \mathbf{M} and $\hat{\mathbf{M}}$ refer to the predicted plane mask and its matched ground truth mask. $\mathbf{S}_{cls}^{\mathbf{M}}$ denotes the semantic score of \mathbf{M} . After that, Hungarian algorithm (Date and Nagi, 2016) is used to search for the best N_{gt} mask pairs with the minimal total matching cost.

Semantic class loss. We aim to ensure that the predicted plane masks within the optimal matching pairs are identified as positive masks, while the other predicted plane masks are identified as negative masks. To achieve that, we use binary cross-entropy loss to construct semantic class loss \mathcal{L}_{cls} , which can be described as:

$$\mathcal{L}_{cls} = -\frac{1}{K} \sum_{i=1}^K [l_{cls_i} \cdot \log(s_i) + (1 - l_{cls_i}) \cdot \log(1 - s_i)], \quad (13)$$

where s_i and l_{cls_i} refers to the semantic score and label of i -th predicted plane mask. Here, $l_{cls_i} = 1$ when the i -th prediction is matched with ground truth, and 0 otherwise.

Edge mask loss. Similar to plane mask loss, we use \mathcal{L}_{BCE}^w and \mathcal{L}_{Dice}^w to formulate the edge mask loss \mathcal{L}_{edge}^w , which can be defined as:

$$\mathcal{L}_{edge}^w = \mathcal{L}_{BCE}^w(\mathbf{M}_{edge}, \hat{\mathbf{M}}_{edge}) + \mathcal{L}_{Dice}^w(\mathbf{M}_{edge}, \hat{\mathbf{M}}_{edge}), \quad (14)$$

where \mathbf{M}_{edge} and $\hat{\mathbf{M}}_{edge}$ refer to the predicted and ground truth edge mask. To generate

$\hat{\mathbf{M}}_{edge}$, we perform neighborhood analysis for each point. If there exist neighbors with different labels, the point is identified as an edge point assigned with label 1; otherwise, it is considered a non-edge point assigned with label 0.

4. Experiments

4.1. Implementation details

Network details. The backbone, built on the PointNet++ (Qi et al., 2017), consists of four Set Abstraction (SA) layers and four Attention-based Feature Propagation (AFP) layers. The SA layers are applied to downsample the input points, with sampling ratio of 1/4 in each layer, and aggregate the features with receptive radius of $[0.05, 0.1]$, $[0.1, 0.2]$, $[0.2, 0.4]$ and $[0.4, 0.8]$. Then, AFP layers are applied to gradually upsample and generate the multi-scale point features. The attention-based modules (in AFP, QRD and EAMM) employ standard transformer blocks (Vaswani et al., 2017), with both input and output dimension set to 256, and the dropout threshold set to 0.3. The edge prediction branch and query semantic branch are essentially two MLPs, with the output dimension set to 1. The dropout threshold is set to 0.1 in both branches.

Training details. The network training was performed under the PyTorch framework using a GeForce RTX 4090 GPU (24GB). The optimization process employs AdamW (Loshchilov et al., 2017) with the learning rate follows a cosine decay schedule to a minimum of 1×10^{-6} . RoofSeg are trained with the maximum 200 epochs, while the batch size is set to 24. To enable batched processing, all input point clouds are uniformly resampled to 2,048 points in training phase.

4.2. Datasets preparation

RoofNTNU benchmark. This is a small-scale real-world benchmark built by Zhang and Fan (2022). It contains 1,032 building roofs from Trondheim city in Norway, which are manually segmented into 3,478 planes. The benchmark is divided into training, validation and test set in an 8:1:1 ratio. In this paper, we merge the training and validation sets, resulting in a combined training set of 933 roofs. Some roof samples of this benchmark are shown in Fig. 5 (the first line).

Roofpc3D benchmark. It is a large-scale synthetic benchmark generated by [Li et al. \(2024\)](#), which contains 15,400 building roofs with annotated plane instance labels. It includes 14 types of roofs, such as pyramid, dormer and cross-hipped, with 1,100 samples of each type. In this benchmark, the maximum number of planes for a single roof sample is 8, while the minimum is 2. Following a ratio of 10:1, the benchmark is divided into a training set of 14,000 roofs and a test set of 1400 roofs. Some roof samples are presented in Fig. 5 (the second line).

Building3D benchmark. This is a real-world benchmark constructed on large-scale 3D urban buildings for roof structure learning, created by [Wang et al. \(2023a\)](#), which comprises the airborne point clouds, wireframe models and surface meshes of 32,618 building roofs from Tallinn city. Based on that, [Li et al. \(2024\)](#) selected 18,708 roofs and manually annotated the ground truth plane labels, thus deriving a new benchmark for roof plane segmentation. The benchmark was split into 16,884 training and 1,824 test samples at an approximate 10:1 ratio. Notably, it is a challenging benchmark due to its more diverse and complex roof types. Some roof samples are presented in Fig. 5 (the third line).

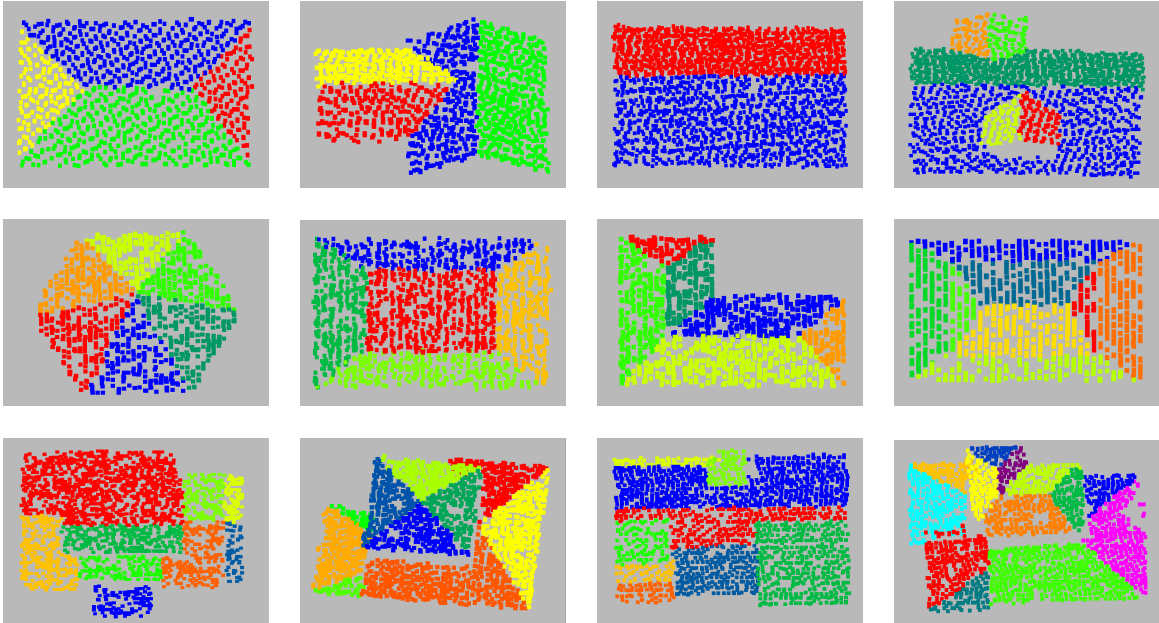


Figure 5: Visualization of some roof samples from RoofNTNU benchmark (the first line), Roofpc3D benchmark (the second line) and Building3D benchmark (the third line). Different colored points on a roof sample denote different planar surfaces.

4.3. Evaluation metrics

For comprehensive evaluation of roof plane segmentation results, we utilize four metrics: mean coverage (mCov), mean weighted coverage (mWCov), mean precision (mPrec), and mean recall (mRec). The complete definitions of these metrics are provided in the paper of Li et al. (2024).

4.4. Comparative experiments

To demonstrate the superiority of RoofSeg, we conducted comparative experiments on three benchmarks with three traditional approaches: Region Growing (Vo et al., 2015), RANSAC (Xu et al., 2015), and GoCoPP (Yu and Lafarge, 2022), as well as three deep learning-based approaches: PointGroup (Jiang et al., 2020), Mask3D (Schult et al., 2023), and DeepRoofPlane (Li et al., 2024). The code for Region Growing and RANSAC is provided by the open-source libraries Open3D ¹ and PCL ², while the code for GoCoPP and three deep learning-based approaches can be obtained from the respective authors' GitHub pages. The quantitative assessment of all comparative approaches and RoofSeg on three benchmarks are presented in Table 1.

Table 1: Quantitative assessment of all comparative approaches and RoofSeg on three benchmarks.

Different approaches	RoofNTNU benchmark				Roofpc3D benchmark				Building3D benchmark			
	mCov	mWCov	mPrec	mRec	mCov	mWCov	mPrec	mRec	mCov	mWCov	mPrec	mRec
Region growing	0.7016	0.7549	0.7586	0.7347	0.7039	0.7458	0.7839	0.7710	0.7341	0.7893	0.8179	0.7847
RANSAC	0.7291	0.7213	0.7457	0.7318	0.7563	0.7608	0.7981	0.7842	0.7635	0.8017	0.8169	0.7980
GoCoPP	0.8092	0.8547	0.8690	0.8319	0.8145	0.8206	0.8741	0.8352	0.8057	0.8542	0.8590	0.8278
PointGroup	0.8164	0.8421	0.8599	0.8328	0.8357	0.8528	0.8819	0.8402	0.8140	0.8359	0.8631	0.8466
Mask3D	0.8803	0.8951	0.9500	0.9018	0.8720	0.9047	0.9425	0.9101	0.8417	0.8862	0.9325	0.8993
DeepRoofPlane	0.9113	0.9374	0.9769	0.9438	0.9234	0.9475	0.9827	0.9501	0.8914	0.9279	0.9760	0.9314
RoofSeg (ours)	0.9589	0.9682	0.9960	0.9818	0.9601	0.9756	0.9998	0.9854	0.9374	0.9637	0.9879	0.9658

From the results in Table 1, it can be found that our network (RoofSeg) achieves the highest scores across all four evaluation metrics. Compared to DeepRoofPlane (Li et al.,

¹Available at <https://github.com/is1-org/Open3D/>.

²Available at <https://github.com/CGAL/cgal/>.

2024), which is the most competitive among all the comparative approaches, RoofSeg leads by 3 to 4 percentage points in Cov, WCov, and mRec, and also shows an improvement of approximately 1.5 percentage points in mPrec. In comparison with the other five approaches, RoofSeg outperforms them significantly in all metrics on three benchmarks. High scores in Cov and WCov indicate that RoofSeg achieves high accuracy in point-level segmentation, while the high scores in mPrec and mRec demonstrate the superior performance of RoofSeg in plane instance-level segmentation.

To qualitatively evaluate different approaches, we present segmentation results of representative roof samples from three benchmarks in Figures 6, 7, and 8. For the RoofNTNU and Roofpc3D benchmarks, Region Growing (Vo et al., 2015) tends to fail at edge regions between adjacent patches (Fig. 6 (B₁)) and produce over-segmented small patches (Fig. 6 (B₂)). RANSAC (Xu et al., 2015) generates numerous spurious planes (Fig. 6 (C₁) and Fig. 7 (C₁)). The results of GoCoPP (Yu and Lafarge, 2022) show inaccurate edge segmentation with misclassified points (outliers) distributed across segmented patches (Fig. 6 (D₁) and (D₂)), while also struggling with under-segmentation issues (Fig. 7 (D₁) and (D₂)). Both PointGroup (Jiang et al., 2020) and Mask3D (Schult et al., 2023) fail to achieve accurate and smooth edge segmentation. Moreover, PointGroup exhibits over-segmentation, which erroneously segments large patches into smaller ones (Fig. 7 (E₁) and (E₂)). Mask3D produces numerous misclassified points and under-segmented patches (Fig. 6 (F₂) and Fig. 7 (F₂)). DeepRoofPlane (Li et al., 2024) achieves better segmentation quality. However, it still generates non-smooth edges at junctions and shows some under-segmented regions (Fig. 6 (G₂) and Fig. 7 (G₂)). RoofSeg achieves the highest-quality segmentation results, with accurate edges, minimal misclassified points and high geometric fidelity. For the more challenging Building3D benchmark (with complex roof structures), all comparative approaches show significantly degraded performance with more severe under- or over-segmentation issues and inaccurate edges. In contrast, RoofSeg achieves optimal results that maximally approximate the ground truth, demonstrating its effectiveness in handling challenging roof samples. Moreover, we also show the urban-scale segmented roofs of RoofSeg on the Building3D benchmark in Fig. 9.

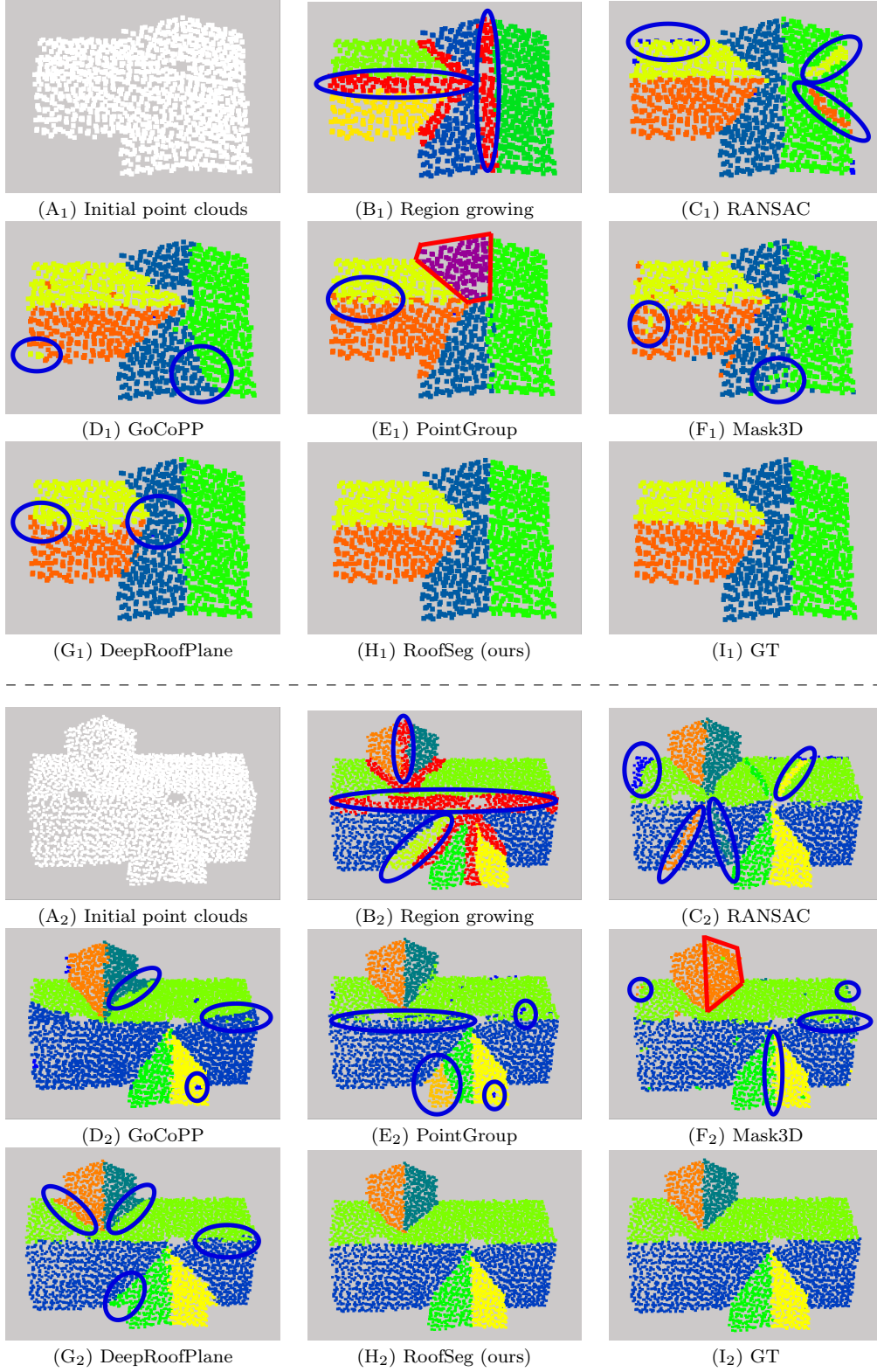


Figure 6: Visual results of roof plane segmentation for all comparative approaches and RoofSeg on the RoofNTNU benchmark. The blue ellipses point out some incorrectly segmented regions. The red wireframes point out some regions with under-segmentation.

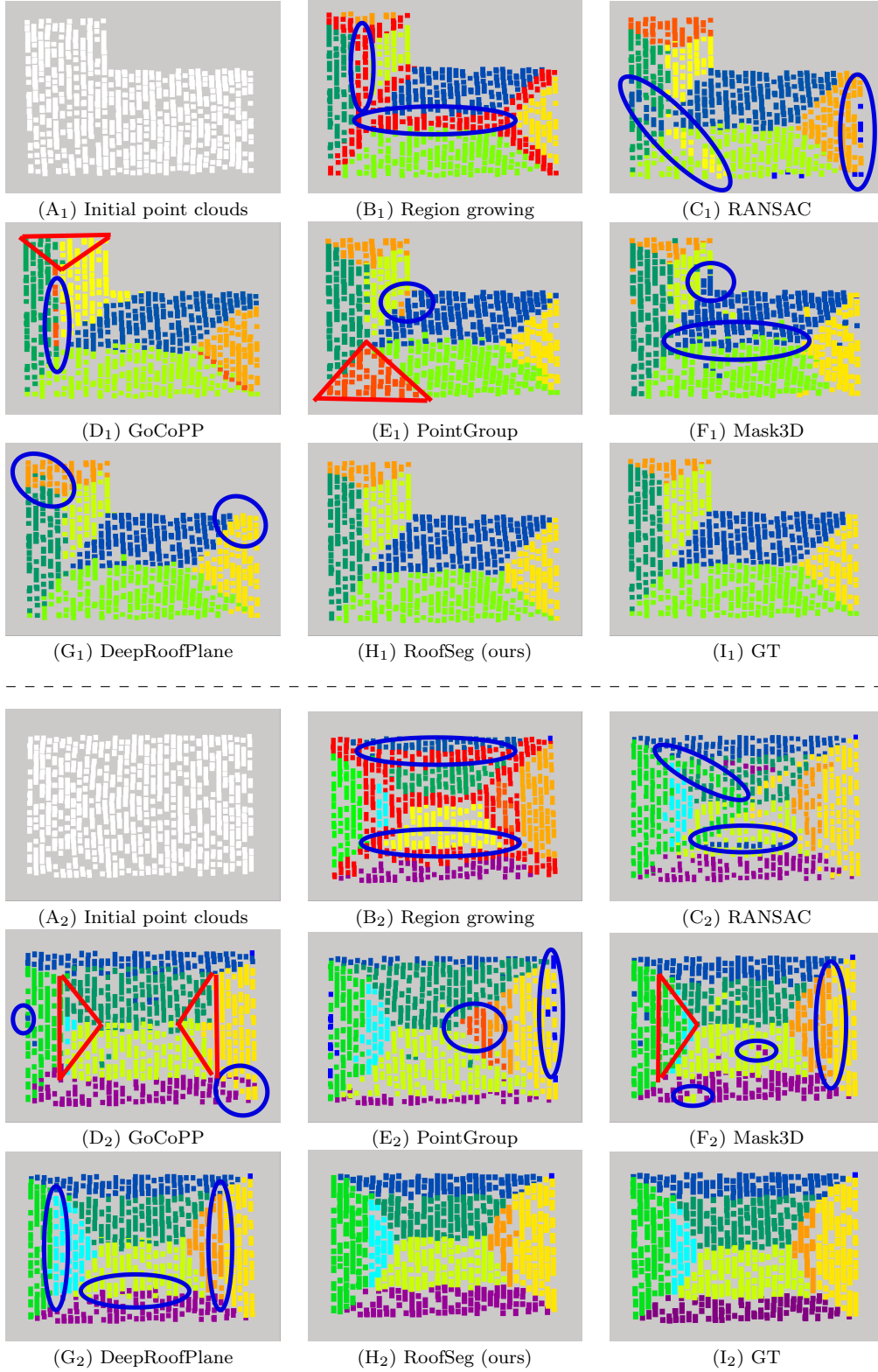


Figure 7: Visual results of roof plane segmentation for all comparative approaches and RoofSeg on the Roofpc3D benchmark. The blue ellipses point out some incorrectly segmented regions. The red wireframes point out some regions with under-segmentation.

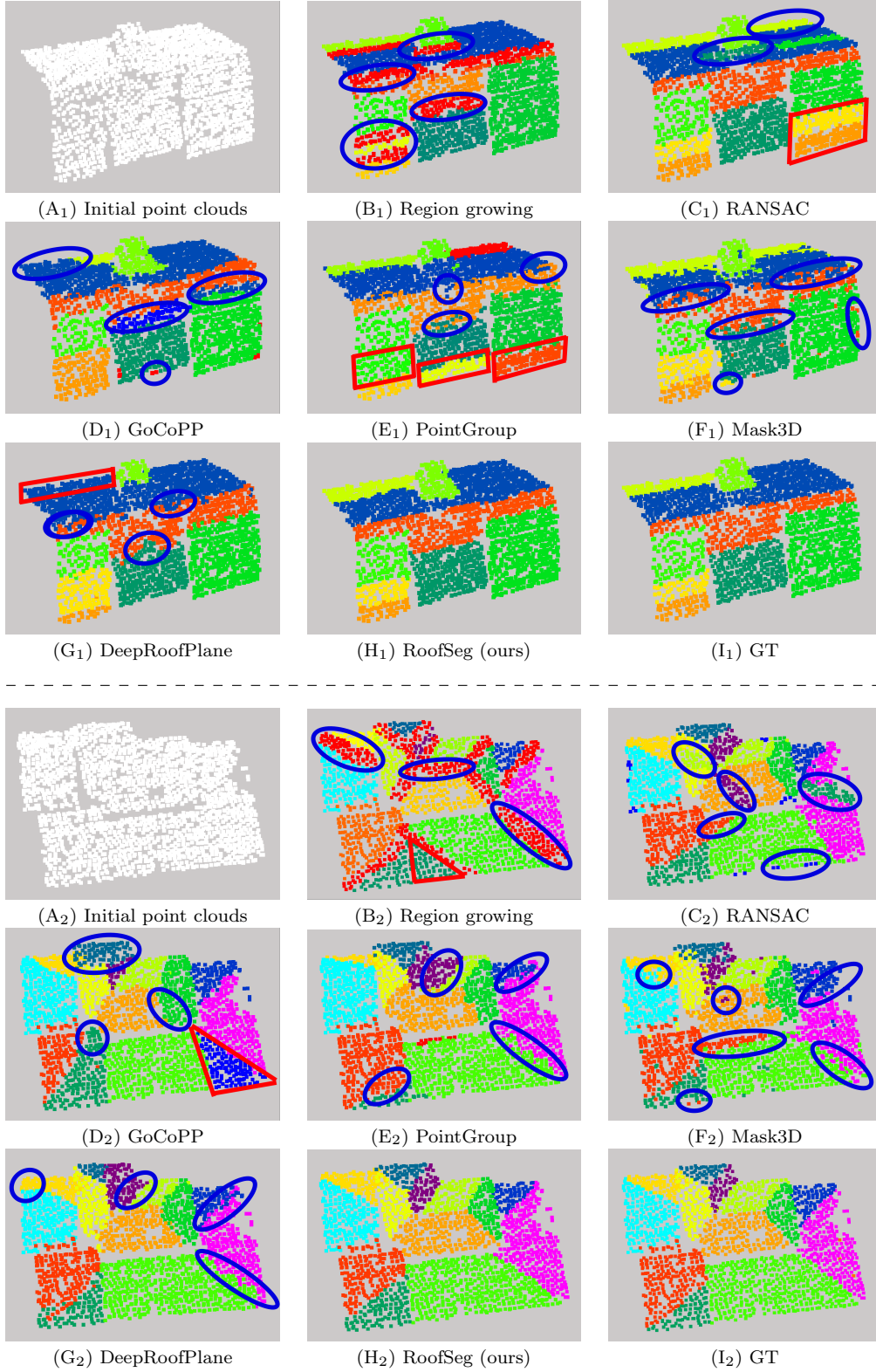


Figure 8: Visual results of roof plane segmentation for all comparative approaches and RoofSeg on the Building3D benchmark. The blue ellipses point out some incorrectly segmented regions. The red wireframes point out some regions with under-segmentation.

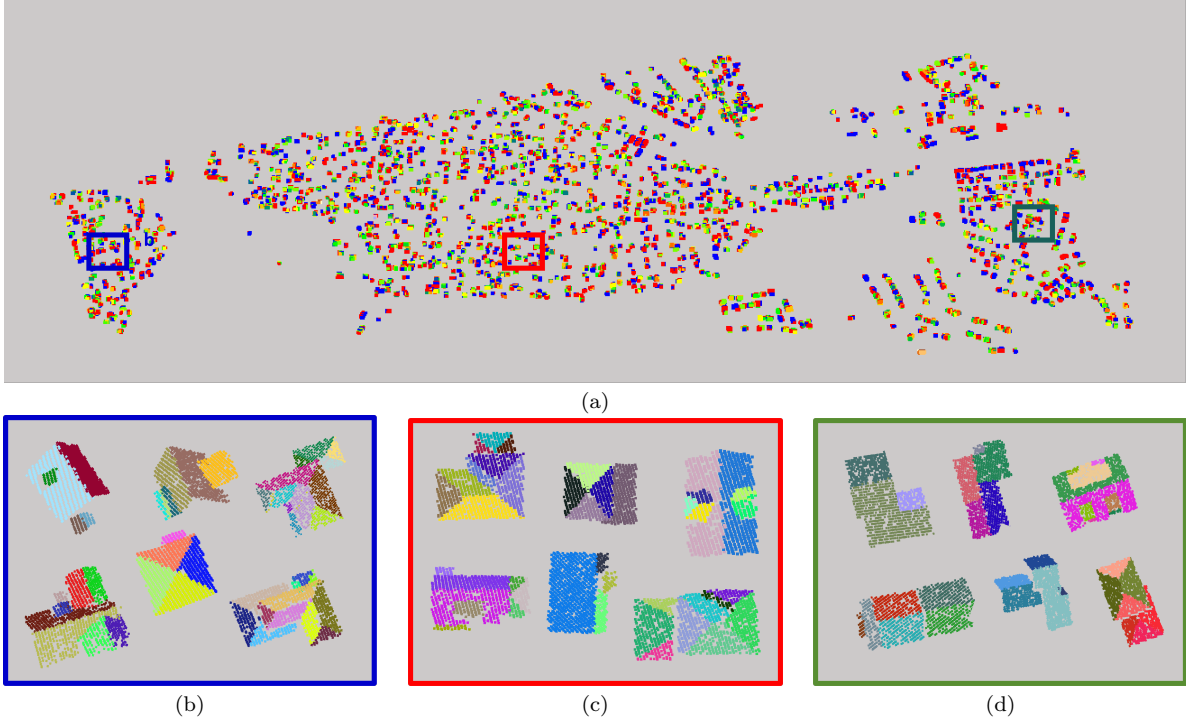


Figure 9: Large scale segmentation results of RoofSeg on the real-world Building3D benchmark. In (a), we present all 1827 segmented roofs in the testing set. (b), (c) and (d) highlight the segmentation results of three local regions, respectively.

4.5. Ablations

The effects of different components. To systematically evaluate the effectiveness of the Edge-Aware Mask Module (EAMM) and the proposed loss function with two key components (\mathcal{L}_{mask}^w and \mathcal{L}_{plane}), we conducted the ablation experiments with 8 control groups (a-h). In these groups, (a-d) and (e-h) are employed to evaluate the network’s performance without and with the EAMM, respectively. To study the impact of different loss components, we set up four loss controls for comparison, including two baselines (conventional mask loss \mathcal{L}_{mask} and adaptive weighting mask loss \mathcal{L}_{mask}^w), along with their variants added with the plane geometric loss \mathcal{L}_{plane} . The quantitative evaluation results are presented in the Table 2. From the table, it can be concluded that EAMM and the proposed loss function (with \mathcal{L}_{mask}^w and \mathcal{L}_{plane}) can both effectively improve the segmentation accuracy. In terms of the Cov metric, using EAMM leads to an improvement of about 4 percentage points on the RoofNTNU and Roofpc3D benchmarks, while the improvement exceeds 5 percentage points on the Building3D benchmark. Besides, compared to the

baseline loss that relies solely on \mathcal{L}_{mask} , using the proposed loss function can achieve an improvement of 3 to 4 percentage points across the three benchmarks. To qualitatively demonstrate the impact of three components (EAMM, \mathcal{L}_{mask}^w and \mathcal{L}_{plane}), we presented the visual segmentation results of two roof samples (from RoofNTNU and Building3D benchmarks, respectively) with different components in Fig. 10. Without EAMM, segmentation accuracy degrades significantly at edge regions. Without \mathcal{L}_{mask}^w , the segmentation results may produce a large number of misclassified points (outliers) across different patches. Without \mathcal{L}_{plane} , misclassified points still occur and under-segmentation could happen, where small patches are incorrectly merged with larger ones, resulting in plane segments with low geometric fidelity, as highlighted by the red wireframes in Fig. 10.

Table 2: Quantitative assessment of RoofSeg using different components on three benchmarks. EAMM denotes Edge-Aware Mask Module, while \mathcal{L}_{mask} , \mathcal{L}_{mask}^w and \mathcal{L}_{plane} represent conventional mask loss, adaptive weighting mask loss and plane geometric loss.

Different components					RoofNTNU benchmark				Roofpc3D benchmark				Building3D benchmark			
	EAMM	\mathcal{L}_{mask}	\mathcal{L}_{mask}^w	\mathcal{L}_{plane}	mCov	mWCov	mPrec	mRec	mCov	mWCov	mPrec	mRec	mCov	mWCov	mPrec	mRec
(a)	×	✓	×	×	0.8747	0.8895	0.9309	0.8911	0.8821	0.9041	0.9510	0.9173	0.8424	0.8736	0.9298	0.8802
(b)	×	×	✓	×	0.8905	0.9101	0.9437	0.9073	0.8943	0.9189	0.9624	0.9317	0.8605	0.8870	0.9398	0.8868
(c)	×	✓	×	✓	0.8836	0.9098	0.9468	0.9147	0.9013	0.9223	0.9689	0.9331	0.8596	0.8941	0.9444	0.8921
(d)	×	×	✓	✓	0.9119	0.9328	0.9666	0.9374	0.9189	0.9397	0.9733	0.9458	0.8878	0.9170	0.9513	0.9179
(e)	✓	✓	×	×	0.9176	0.9388	0.9899	0.9357	0.9206	0.9431	0.9876	0.9635	0.8954	0.9231	0.9696	0.9270
(f)	✓	×	✓	×	0.9325	0.9514	0.9926	0.9604	0.9385	0.9580	0.9980	0.9711	0.9181	0.9432	0.9781	0.9394
(g)	✓	✓	×	✓	0.9297	0.9505	0.9949	0.9525	0.9426	0.9621	0.9974	0.9794	0.9106	0.9437	0.9755	0.9435
(h)	✓	×	✓	✓	0.9589	0.9682	0.9960	0.9818	0.9601	0.9756	0.9998	0.9854	0.9374	0.9637	0.9879	0.9658

The effects of different backbones. We applied two prevalent feature extraction backbones in 3D domain, i.e., 3D U-Net (Choy et al., 2019) and PointNet++ (Qi et al., 2017). For 3D U-Net, we used a grid size of 0.02m for voxelization according to the point density of three benchmarks, while the other parameters are consistent with Choy et al. (2019). For PointNet++, we implemented two variants: 1) the baseline with standard Feature Propagation (FP), and 2) the enhanced version with Attention-based Feature Propagation (AFP). The metric results on three benchmarks are given in Table 3. The PointNet++ variant with AFP gains the best results on all four metrics. For the Cov metric, it shows an improvement of more than 3 percentage points compared to 3D U-

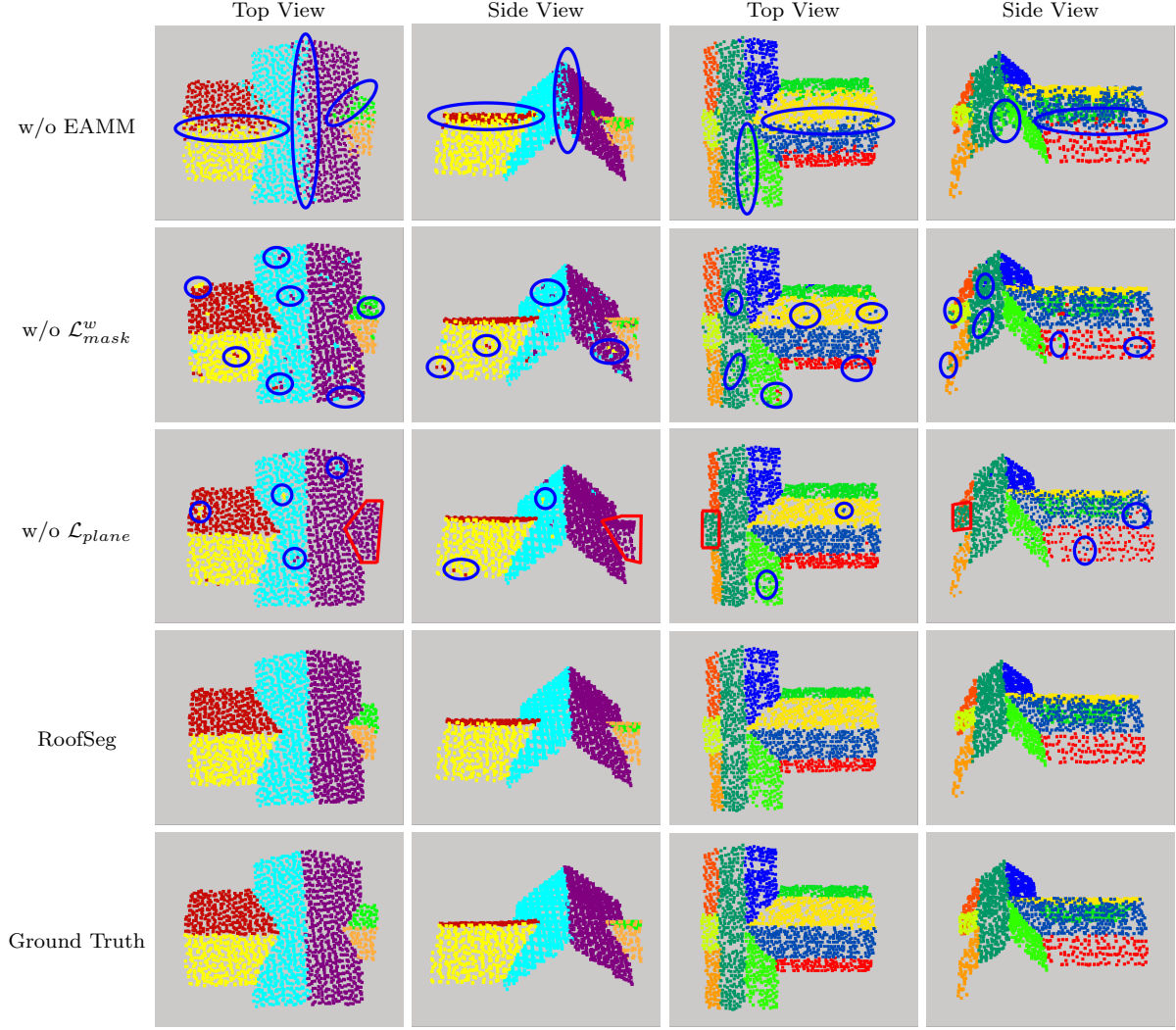


Figure 10: Segmentation results of two roof samples using the proposed network with different components. The first, second and third rows represent the segmentation results without using BMM, adaptive mask loss \mathcal{L}_{mask}^w and plane geometric loss \mathcal{L}_{plane} , respectively. The forth row represents the segmentation results using all three components, while the last row represents the Ground Truth. The blue ellipses and red wireframes point out some incorrectly segmented regions.

Net, and nearly a 1-point improvement compared to the PointNet++ baseline. Similar trends hold for other metrics as well.

The effects of using different numbers of plane queries for segmentation.

We trained the network with 16, 32, 64 and 128 plane queries for three benchmarks, respectively. The metric results are provided in Table 4. On the RoofNTNU and Roofpc3D benchmarks, the network trained with 32 plane queries achieves the highest metric scores, while more plane queries (64) are required for achieving the best results on the Build-

Table 3: Quantitative assessment of RoofSeg using different backbones on three benchmarks. FP and AFP denotes the standard and attention-based feature propagation applied in PointNet++, respectively.

Different backbones		RoofNTNU benchmark				Roofpc3D benchmark				Building3D benchmark			
		mCov	mWCov	mPrec	mRec	mCov	mWCov	mPrec	mRec	mCov	mWCov	mPrec	mRec
3D U-Net		0.9248	0.9423	0.9670	0.9473	0.9209	0.9455	0.9786	0.9535	0.9041	0.9274	0.9597	0.9332
PointNet++	w/ FP	0.9503	0.9621	0.9899	0.9757	0.9528	0.9664	0.9925	0.9801	0.9283	0.9540	0.9790	0.9602
	w/ AFP	0.9589	0.9682	0.9960	0.9818	0.9601	0.9756	0.9998	0.9854	0.9374	0.9637	0.9879	0.9658

ing3D benchmark, which contains complex roof structures with more planar patches. In addition, from the Table 4, we observed that a small number (16) or a large number (128) of plane queries could weaken the performance of the network. This is because with few queries, under-segmentation may occur, potentially missing small planar patches. On the other hand, with excessive queries, redundant predictions are likely to arise, thus leading to over-segmentation.

Table 4: Quantitative assessment of RoofSeg using different numbers of plane queries on three benchmarks.

Different numbers of plane queries	RoofNTNU benchmark				Roofpc3D benchmark				Building3D benchmark			
	mCov	mWCov	mPrec	mRec	mCov	mWCov	mPrec	mRec	mCov	mWCov	mPrec	mRec
16	0.9278	0.9412	0.9743	0.9619	0.9388	0.9552	0.9840	0.9538	0.9136	0.9383	0.9701	0.9457
32	0.9589	0.9682	0.9960	0.9818	0.9601	0.9756	0.9998	0.9854	0.9301	0.9590	0.9820	0.9613
64	0.9438	0.9545	0.9792	0.9672	0.9506	0.9614	0.9822	0.9680	0.9374	0.9637	0.9879	0.9658
128	0.9024	0.9305	0.9572	0.9238	0.9175	0.9386	0.9690	0.9228	0.8912	0.9179	0.9587	0.9204

The effects of adaptive weighting loss calculation with varied numbers of nearest neighbors. As described in the Section 3.4, to calculate the adaptive weighting mask loss, we first performed neighborhood analysis for each point based on the initial plane mask to identify potential misclassified points, whose labels do not align with the majority of their neighbors, and then adaptively computed their weights. To investigate the effect of selecting different numbers of nearest neighbors (N_{knn}), we conducted corresponding experiments on three benchmarks, with N_{knn} set to 10, 20, 30, 40, and 50, respectively. As shown in Table 5, the results across all groups are very close on all four metrics, with the largest gap being less than 0.5 percentage points. From that observa-

tion, it can be concluded that our network is not sensitive to this hyperparameter. In experiments, we empirically set N_{knn} to 30.

Table 5: Quantitative assessment of RoofSeg using varied numbers of nearest neighbors (N_{knn}) in adaptive weighting loss calculation on three benchmarks.

Variation in N_{knn}	RoofNTNU benchmark				Roofpc3D benchmark				Building3D benchmark			
	mCov	mWCov	mPrec	mRec	mCov	mWCov	mPrec	mRec	mCov	mWCov	mPrec	mRec
10	0.9576	0.9639	0.9906	0.9769	0.9560	0.9723	0.9947	0.9806	0.9325	0.9588	0.9840	0.9596
20	0.9573	0.9652	0.9963	0.9802	0.9600	0.9734	0.9950	0.9843	0.9357	0.9597	0.9851	0.9609
30	0.9589	0.9682	0.9960	0.9818	0.9601	0.9756	0.9998	0.9854	0.9374	0.9637	0.9879	0.9658
40	0.9569	0.9675	0.9954	0.9793	0.9587	0.9750	0.9987	0.9832	0.9329	0.9639	0.9857	0.9625
50	0.9547	0.9645	0.9937	0.9774	0.9571	0.9711	0.9941	0.9815	0.9338	0.9605	0.9839	0.9613

4.6. Efficiency and accuracy analysis

The effects of different numbers of Query Refinement Decoders (QRD). In our network, we employ transformer decoders to hierarchically refine the plane queries with the multi-scale point features. To evaluate the effects of varied decoder numbers (N_{dec}) on the performance of RoofSeg, we conducted several experiments, with N_{dec} set to 4, 8 and 12 respectively. As shown in Table 6, with the number of decoders increases, both the parameters and computational complexity of the network rise significantly, leading to increased time costs and resource consumption. From Table 7, we observed that using 8 decoders can achieve better performance compared to using 4 decoders, while further increasing N_{dec} does not provide a significant improvement. Thereby, we empirically set N_{dec} to 8 for our network under the consideration of both computational efficiency and segmentation accuracy.

The effects of different point features (multi-scale/full resolution) applied for cross-attention operation in QRD. Notably, in each QRD, the standard cross-attention operation has quadratic computational complexity $O(KN)$ with respect to the query number K and point number N , where $K \ll N$. Therefore, the key factor affecting the computational efficiency of each QRD is the number of input points. Compared to use point features with full resolution in all decoders, using multi-scale features across different decoders can greatly reduce the computational costs, as demonstrated in the

Table 6: Efficiency analysis of RoofSeg employing different numbers of Query Refinement Decoders (QRD). # Para. represents the total parameter amount of RoofSeg. FLOPs represents the count of floating-point calculations performed during the forward pass in one second. Inference time represents the average processing time per batch (batch size=24), while GPU memory denotes the memory consumption on a single GPU during training.

Decoder numbers	# Para.(MB)	FLOPs (GB)	Inference time (s)	GPU memory (MB)
4	22.855	16.095	1.633	13303.05
8	32.926	18.118	2.944	14091.12
12	42.996	20.141	4.174	15262.72

Table 7: Accuracy analysis of RoofSeg employing different numbers of Query Refinement Decoders (QRD) on three benchmarks.

Decoder numbers	RoofNTNU benchmark				Roofpc3D benchmark				Building3D benchmark			
	mCov	mWCov	mPrec	mRec	mCov	mWCov	mPrec	mRec	mCov	mWCov	mPrec	mRec
4	0.9178	0.9221	0.9674	0.9303	0.9246	0.9410	0.9615	0.9347	0.8914	0.9139	0.9607	0.9299
8	0.9589	0.9682	0.9960	0.9818	0.9601	0.9756	0.9998	0.9854	0.9374	0.9637	0.9879	0.9658
12	0.9593	0.9671	0.9964	0.9813	0.9597	0.9731	0.9999	0.9865	0.9369	0.9641	0.9873	0.9642

Table 8. From the table, it can also be found that with the growth of input point count, the efficiency advantage of using multi-scale features becomes more evident. Regarding the segmentation accuracy, these two strategies achieve very close performance, as shown in Table 9. Given these results, it can be concluded that using multi-scale features is a better choice, which can achieve competitive performance on segmentation accuracy while ensuring higher network efficiency.

Table 8: Efficiency analysis of RoofSeg using different point features (multi-scale/full resolution) applied for cross-attention operations in QRD. In this table, the batch size is set to 1, given the maximum GPU memory may not enough for processing multi-batch inputs with large point numbers.

Input point numbers	Multi-scale features			Full resolution features		
	FLOPs (GB)	Infer. time (s)	GPU mem. (MB)	FLOPs (GB)	Infer. time (s)	GPU mem. (MB)
2048	18.118	0.365	611.95	22.257	0.372	854.45
4096	35.466	0.386	1607.49	45.981	0.403	2223.40
6044	59.391	0.416	3150.46	75.969	0.449	4216.25
8192	94.164	0.459	5516.11	117.428	0.497	7088.76

Table 9: Accuracy analysis of RoofSeg using different point features (multi-scale/full resolution) applied for cross-attention operations in QRD on three benchmarks.

Different point features	RoofNTNU benchmark				Roofpc3D benchmark				Building3D benchmark			
	mCov	mWCov	mPrec	mRec	mCov	mWCov	mPrec	mRec	mCov	mWCov	mPrec	mRec
Multi-scale feat.	0.9589	0.9682	0.9960	0.9818	0.9601	0.9756	0.9998	0.9854	0.9374	0.9637	0.9879	0.9658
Full resolution feat.	0.9587	0.9683	0.9948	0.9807	0.9605	0.9761	0.9970	0.9839	0.9380	0.9618	0.9864	0.9662

5. Conclusion

In this work, we develop an edge-aware transformer-based network, named RoofSeg, for end-to-end segmenting roof planes from airborne LiDAR point clouds. Without any parameter-sensitive clustering-based techniques or post-processing steps, the proposed network can achieve roof plane segmentation in a truly end-to-end manner, by directly predicting the instance masks of the potential planes in point clouds. To improve the segmentation accuracy near the edge regions, we design an Edge-Aware Mask Module (EAMM). In this module, we utilize the critical geometric cue, namely point-to-plane distance, to enhance the discriminativity at the edge points and facilitate the further plane mask refinement. In addition, we propose a novel loss function for supervising the plane mask predictions: (1) an adaptive weighting strategy is introduced into the mask loss for eliminating the influence of the misclassified points; (2) a geometric plane loss is added into the network training to ensure the predicted plane segments with high geometric fidelity. The extensive experiments on three benchmarks have demonstrated the proposed network can segment roof planes with accurate edges, minimal misclassified points and high geometric fidelity, while achieving the new state-of-the-art performance compared to current roof plane segmentation approaches.

Nevertheless, our network still can be improved in terms of efficiency, as it requires a number of decoders to ensure optimal segmentation performance. In future work, we will focus on developing a more efficient network for extracting roof planes based on the current framework.

Acknowledgements

This work was partially funded by the National Natural Science Foundation of China (No.U22A2009, No.42271445, No.42101440), the Natural Science Foundation of Hubei Province (No.2025AFB491), the Shenzhen Science and Technology Program (JCYJ2023 0807090206013).

References

- Boykov, Y., Veksler, O., 2006. Graph cuts in vision and graphics: Theories and applications, in: Handbook of Mathematical Models in Computer Vision, pp. 79–96.
- Canaz Sevgen, S., Karsli, F., 2020. An improved RANSAC algorithm for extracting roof planes from airborne LiDAR data. *The Photogrammetric Record* 35, 40–57.
- Cao, Y., Cao, J., Xing, L., Zhu, B., Bao, Q., Li, T., Wang, Q., 2025. An enhanced-RANSAC-fusion and Kd-tree-filtering pipeline method for multi-scale 3D substation components extraction. *IEEE Sensors Journal* 25, 30897–30905.
- Cao, Y., Wang, Y., Xue, Y., Zhang, H., Lao, Y., 2022. FEC: Fast Euclidean clustering for point cloud segmentation. *Drones* 6, 325.
- Chen, F., Xie, F., Sun, L., Gu, Y., Zhang, Z., Chen, J., Zhang, J., Yi, M., 2024. Point cloud segmentation algorithm based on improved Euclidean clustering. *IEEE Access* 12, 152959–152971.
- Chen, X., Mao, J., Zhao, B., Wu, C., Qin, M., 2025. Facet-segmentation of point cloud based on multiscale hypervoxel region growing. *Journal of the Indian Society of Remote Sensing* , 1–22.
- Cheng, B., Misra, I., Schwing, A.G., Kirillov, A., Girdhar, R., 2022. Masked-attention mask transformer for universal image segmentation, in: IEEE/CVF Conference on Computer Vision and Pattern Recognition (CVPR), pp. 1290–1299.

- Cheng, B., Schwing, A., Kirillov, A., 2021. Per-pixel classification is not all you need for semantic segmentation, in: *Advances in Neural Information Processing Systems (NeurIPS)*, pp. 17864–17875.
- Choy, C., Gwak, J., Savarese, S., 2019. 4D spatio-temporal convnets: Minkowski convolutional neural networks, in: *IEEE/CVF Conference on Computer Vision and Pattern Recognition (CVPR)*, pp. 3075–3084.
- Czerniawski, T., Sankaran, B., Nahangi, M., Haas, C., Leite, F., 2018. 6D DBSCAN-based segmentation of building point clouds for planar object classification. *Automation in Construction* 88, 44–58.
- Date, K., Nagi, R., 2016. GPU-accelerated Hungarian algorithms for the linear assignment problem. *Parallel Computing* 57, 52–72.
- Fang, Z., Zhuang, C., Lu, Z., Wang, Y., Liu, L., Xiao, J., 2025. BGPSeg: Boundary-guided primitive instance segmentation of point clouds. *IEEE Transactions on Image Processing (TIP)* 34, 1454–1468.
- Gu, Y., Cao, Z., Dong, L., 2017. A hierarchical energy minimization method for building roof segmentation from airborne LiDAR data. *Multimedia Tools and Applications (MTA)* 76, 4197–4210.
- He, Y., Zhang, C., Fraser, C.S., 2013. A line-based spectral clustering method for efficient planar structure extraction from LiDAR data. *ISPRS Annals of the Photogrammetry, Remote Sensing and Spatial Information Sciences* 2, 103–108.
- Huang, J., Stoter, J., Peters, R., Nan, L., 2022. City3D: Large-scale building reconstruction from airborne LiDAR point clouds. *Remote Sensing* 14, 2254.
- Huang, J., Zhang, Y., Sun, M., 2021. PrimitiveNet: Primitive instance segmentation with local primitive embedding under adversarial metric, in: *IEEE/CVF International Conference on Computer Vision (ICCV)*, pp. 15343–15353.

- Jiang, L., Zhao, H., Shi, S., Liu, S., Fu, C.W., Jia, J., 2020. PoinGroup: Dual-set point grouping for 3D instance segmentation, in: IEEE/CVF Conference on Computer Vision and Pattern Recognition (CVPR), pp. 4867–4876.
- Khaloo, A., Lattanzi, D., 2017. Robust normal estimation and region growing segmentation of infrastructure 3D point cloud models. *Advanced Engineering Informatics (AEI)* 34, 1–16.
- Lai, X., Yuan, Y., Chu, R., Chen, Y., Hu, H., Jia, J., 2023. Mask-attention-free transformer for 3D instance segmentation, in: IEEE/CVF International Conference on Computer Vision (ICCV), pp. 3693–3703.
- Li, L., Li, Q., Xu, G., Zhou, P., Tu, J., Li, J., Li, M., Yao, J., 2024. A boundary-aware point clustering approach in Euclidean and embedding spaces for roof plane segmentation. *ISPRS Journal of Photogrammetry and Remote Sensing* 218, 518–530.
- Li, L., Yang, F., Zhu, H., Li, D., Li, Y., Tang, L., 2017. An improved RANSAC for 3D point cloud plane segmentation based on normal distribution transformation cells. *Remote Sensing* 9, 433.
- Li, L., Yao, J., Tu, J., Liu, X., Li, Y., Guo, L., 2020. Roof plane segmentation from airborne LiDAR data using hierarchical clustering and boundary relabeling. *Remote Sensing* 12, 1363.
- Li, Y., Liu, S., Yang, X., Guo, J., Guo, J., Guo, Y., 2023. Surface and edge detection for primitive fitting of point clouds, in: ACM SIGGRAPH 2023 conference proceedings, pp. 1–10.
- Liu, K., Ma, H., Zhang, L., Liang, X., Chen, D., Liu, Y., 2023. Roof segmentation from airborne LiDAR using octree-based hybrid region growing and boundary neighborhood verification voting. *IEEE Journal of Selected Topics in Applied Earth Observations and Remote Sensing (J-STARS)* 16, 2134–2146.

- Liu, Y., Obukhov, A., Wegner, J.D., Schindler, K., 2024. Point2Building: Reconstructing buildings from airborne LiDAR point clouds. *ISPRS Journal of Photogrammetry and Remote Sensing* 215, 351–368.
- Liu, Z., Wang, J., Liu, W., 2005. Building extraction from high resolution imagery based on multi-scale object oriented classification and probabilistic Hough Transform, in: *International Geoscience and Remote Sensing Symposium (IGARSS)*, pp. 2250–2253.
- Loshchilov, I., Hutter, F., et al., 2017. Fixing weight decay regularization in Adam. *arXiv preprint arXiv:1711.05101* 5, 5.
- Miao, Y., Li, S., Wang, L., Li, H., Qiu, R., Zhang, M., 2023. A single plant segmentation method of maize point cloud based on Euclidean clustering and K-means clustering. *Computers and Electronics in Agriculture* 210, 107951.
- Misra, I., Girdhar, R., Joulin, A., 2021. An end-to-end transformer model for 3D object detection, in: *IEEE/CVF International Conference on Computer Vision (ICCV)*, pp. 2906–2917.
- Overby, J., Bodum, L., Kjems, E., Iisoe, P., 2004. Automatic 3D building reconstruction from airborne laser scanning and cadastral data using Hough Transform. *International Archives of Photogrammetry, Remote Sensing and Spatial Information Sciences* 34, 296–301.
- Poux, F., Mattes, C., Selman, Z., Kobbelt, L., 2022. Automatic region-growing system for the segmentation of large point clouds. *Automation in Construction* 138, 104250.
- Qi, C.R., Yi, L., Su, H., Guibas, L.J., 2017. PointNet++: Deep hierarchical feature learning on point sets in a metric space, in: *Advances in Neural Information Processing Systems (NeurIPS)*, pp. 5099–5108.
- Roh, W., Jung, H., Nam, G., Yeom, J., Park, H., Yoon, S.H., Kim, S., 2024. Edge-aware 3D instance segmentation network with intelligent semantic prior, in: *IEEE/CVF Conference on Computer Vision and Pattern Recognition (CVPR)*, pp. 20644–20653.

- Schnabel, R., Wahl, R., Klein, R., 2007. Efficient RANSAC for point-cloud shape detection. *Computer Graphics Forum* 26, 214–226.
- Schult, J., Engelmann, F., Hermans, A., Litany, O., Tang, S., Leibe, B., 2023. Mask3D: Mask transformer for 3D semantic instance segmentation, in: *IEEE International Conference on Robotics and Automation (ICRA)*, pp. 8216–8223.
- Sun, J., Qing, C., Tan, J., Xu, X., 2023. Superpoint transformer for 3D scene instance segmentation, in: *AAAI Conference on Artificial Intelligence*, pp. 2393–2401.
- Sun, X., Guo, B., Li, C., Sun, N., Wang, Y., Yao, Y., 2024. Semantic segmentation and roof reconstruction of urban buildings based on LiDAR point clouds. *ISPRS International Journal of Geo-Information* 13, 19.
- Tarsha-Kurdi, F., Landes, T., Grussenmeyer, P., 2007. Hough-transform and extended RANSAC algorithms for automatic detection of 3D building roof planes from LiDAR data, in: *ISPRS Workshop on Laser Scanning*, pp. 407–412.
- Vaswani, A., Shazeer, N., Parmar, N., Uszkoreit, J., Jones, L., Gomez, A.N., Kaiser, Ł., Polosukhin, I., 2017. Attention is all you need, in: *Advances in Neural Information Processing Systems (NeurIPS)*, pp. 1–11.
- Vo, A.V., Truong-Hong, L., Laefer, D.F., Bertolotto, M., 2015. Octree-based region growing for point cloud segmentation. *ISPRS Journal of Photogrammetry and Remote Sensing* 104, 88–100.
- Wang, C., Ji, M., Wang, J., Wen, W., Li, T., Sun, Y., 2019. An improved DBSCAN method for LiDAR data segmentation with automatic Eps estimation. *Sensors* 19, 172.
- Wang, R., Huang, S., Yang, H., 2023a. Building3D: A urban-scale dataset and benchmarks for learning roof structures from point clouds, in: *IEEE/CVF International Conference on Computer Vision (ICCV)*, pp. 20076–20086.

- Wang, S., Qin, F., Tong, Y., Shang, X., Zhang, Z., 2023b. Probabilistic boundary-guided point cloud primitive segmentation network. *IEEE Transactions on Instrumentation and Measurement* 72, 1–13.
- Wang, W., Zhang, Y., Ge, G., Jiang, Q., Wang, Y., Hu, L., 2023c. Indoor point cloud segmentation using a modified region growing algorithm and accurate normal estimation. *IEEE Access* 11, 42510–42520.
- Wang, X., Ji, S., 2021. Roof plane segmentation from LiDAR point cloud data using region expansion based L0 gradient minimization and graph cut. *IEEE Journal of Selected Topics in Applied Earth Observations and Remote Sensing (J-STARS)* 14, 10101–10116.
- Wu, H., Zhang, X., Shi, W., Song, S., Cardenas-Tristan, A., Li, K., 2019. An accurate and robust region-growing algorithm for plane segmentation of TLS point clouds using a multiscale tensor voting method. *IEEE Journal of Selected Topics in Applied Earth Observations and Remote Sensing (J-STARS)* 12, 4160–4168.
- Xu, B., Jiang, W., Shan, J., Zhang, J., Li, L., 2015. Investigation on the weighted RANSAC approaches for building roof plane segmentation from LiDAR point clouds. *Remote Sensing* 8, 5.
- Xu, G., You, S., Liu, K., Li, L., Yao, J., 2025. A coarse-to-fine boundary relabeling approach for roof plane segmentation. *IEEE Geoscience and Remote Sensing Letters* 22, 1–5.
- Xu, J., Li, J., 2023. Optimal RANSAC method for segmentation of complex building roof planes. *Geomatics and Information Science of Wuhan University* 48, 1531–1537.
- Yan, J., Shan, J., Jiang, W., 2014. A global optimization approach to roof segmentation from airborne LiDAR point clouds. *ISPRS Journal of Photogrammetry and Remote Sensing* 94, 183–193.

- Yan, S., Yang, Z., Ma, C., Huang, H., Vouga, E., Huang, Q., 2021. HpNet: Deep primitive segmentation using hybrid representations, in: IEEE/CVF International Conference on Computer Vision (ICCV), pp. 2753–2762.
- Yu, M., Lafarge, F., 2022. Finding good configurations of planar primitives in unorganized point clouds, in: IEEE/CVF Conference on Computer Vision and Pattern Recognition (CVPR), pp. 6367–6376.
- Zeng, C., Qi, X., Chen, C., Sun, K., Zhang, W., Liu, Y., Meng, Y., Yang, B., 2025. SPPSFormer: High-quality superpoint-based transformer for roof plane instance segmentation from point clouds. arXiv preprint arXiv:2505.24475 .
- Zhang, C., Fan, H., 2022. An improved multi-task pointwise network for segmentation of building roofs in airborne laser scanning point clouds. *The Photogrammetric Record* 37, 260–284.
- Zhang, L., Li, Z., Li, A., Liu, F., 2018. Large-scale urban point cloud labeling and reconstruction. *ISPRS Journal of Photogrammetry and Remote Sensing* 138, 86–100.
- Zhao, W., Persello, C., Stein, A., 2022. Extracting planar roof structures from very high resolution images using graph neural networks. *ISPRS Journal of Photogrammetry and Remote Sensing* 187, 34–45.